Environmental Science & Technology

pubs.acs.org/est

Article

Modeling Study of Selenium Migration Behavior in Wet Flue Gas Desulfurization Spray Towers

Renjie Zou, Guangqian Luo,* Can Fang, Haoyu Zhang, Zehua Li, Hongyun Hu, Xian Li, and Hong Yao*

Cite This: *Environ. Sci. Technol.* 2020, 54, 16128−16137

Read Online

ACCESS | Metrics & More | Article Recommendations | Supporting Information

ABSTRACT: Wet flue gas desulfurization (WFGD) system is the core equipment for removing SO_2 from coal-fired power plants, and it also has an important synergistic effect on the removal of selenium. However, the removal efficiency of Se across WFGD systems is not as expected, and it varies greatly in different coal-fired units (12.5−96%). In this study, a mathematical model was established to quantitatively describe the selenium migration behavior in WFGD spray towers, including the conversion of gaseous selenium to particulate selenium and the capture of gaseous SeO_2 and particles by droplets. The calculation results show that the behavior of selenium in the spray tower can be divided into three stages: preparation, condensation, and removal. The condensation stage significantly affected the selenium distribution and its total removal efficiency. Furthermore, five factors which may affect the selenium behavior were investigated. Among them, the inlet particle size distribution and the droplet temperature had great impacts on the outlet selenium concentration, which may be the reason for the unstable selenium removal efficiencies. This study can help in understanding the migration process of selenium in WFGD spray towers and provide some guidance for the development of specific selenium control technologies.

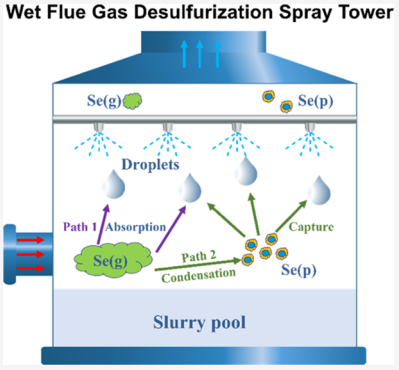

1. INTRODUCTION

Pollutant emissions from coal-fired power plants are of serious concern because of their severe impact on human health and ecological environment. Nowadays, primary pollutants from coal burning, such as SO_2, NO_x, CO_2, particulate matter (PM), and Hg, have been intensively investigated, and a series of control technologies or strategies have been proposed.[1−5] Minor trace metals in coal increasingly attract academic attention.[6−8] Selenium is one of the trace metals in coal. Owing to its high volatility, selenium is almost completely released during the high-temperature burning process,[9,10] which makes it easy to be exhausted into the atmosphere. Excess discharge of selenium is a disaster for aquatic ecosystems, which can cause deformity or even extinction of fishes.[11,12] The Environmental Protection Agency (EPA) of U.S. government regulated the emission limit of selenium, which was 5×10^{-2} lb/GW h for new-built coal-fired units.[13] Thus, it is urgent to develop selenium control technologies for coal-fired power plants.

Selenium in coal is first released out as selenium dioxide under high-temperature condition,[14] and it is called as gaseous Se [expressed as Se(g)]. With the flue gas flowing and cooling down, part of gaseous Se will condense on the fly ash or associate with its Fe/Ca active sites.[15,16] This part of selenium is called as particulate-bound Se [expressed as Se(p)]. The particulate-bound Se can be removed by existing dust collection devices, such as electrostatic precipitators or fabric filters.[17−19] Owing to the similarities between SeO_2 and SO_2, which are both acidic and water-soluble, wet flue gas desulfurization (WFGD) devices have some synergistic removal effects on SeO_2.[20] WFGD devices are the key for SO_2 removal in coal-fired power plants. When the flue gas flows through the WFGD scrubber, it comes in contact with the dense alkaline droplets, and SO_2 can be efficiently washed out. The removal efficiency of SO_2 by WFGD is stable and usually varies from 92 to 98% or higher.[21,22] However, the removal of SeO_2 by WFGD is not as expected. Based on our survey of previous literature, the removal efficiency of selenium by WFGD was found to be 12.5−82.12%.[17−19,23−25] Senior et al. provided some full-scale data in their research, and the efficiency was 53−96%.[26,27] The huge discrepancy of Se removal efficiency among different coal-fired units may be due to the unique characteristic of selenium. However, the selenium behaviors in the flue gas across WFGD systems have not been well understood.

One of the significant differences between SO_2 and SeO_2 is condensation characteristic. Although the vapor pressure of SeO_2 is relatively high compared with other heavy metal elements in coal,[28] part of gaseous Se will condense when the flue gas cools down. Generally, the gas temperature in the inlet

Received: July 21, 2020
Revised: October 13, 2020
Accepted: October 13, 2020
Published: October 23, 2020

https://dx.doi.org/10.1021/acs.est.0c04700
Environ. Sci. Technol. 2020, 54, 16128−16137

of WFGD tower is about 90−110 °C, and it is about 50−60 °C in the outlet. The saturation concentration of SeO_2 decreases rapidly with the flue gas cooling down. A field research was conducted by Senior et al. on a 900 MW coal-fired power plant, and they found the conversion of selenium from gas to particles via physical condensation.[26] The occurrence of condensation may be the main difference between the behaviors of SeO_2 and SO_2, and it may be the possible cause for the unstable selenium removal efficiency.

Model research is a common method to investigate pollutant behavior. A model was created by Senior et al. to calculate the interactions between Se and fly ash, and both heterogeneous condensation and surface reaction were considered.[16] Zhu et al. provided a concise model to describe the absorption process of SO_2 in the WFGD spray tower based on the two-film theory.[29] A one-dimensional model was established by Chen et al. to predict the slurry temperature in the WFGD spray tower.[30]

In this study, a mathematic model was established to describe the selenium migration behaviors in the WFGD tower. The conversion of gaseous Se to particulate-bound Se by condensation was considered. This model presented detailed migration paths of selenium among gaseous, particulate, and liquid phases. Besides, the effects of several key parameters on Se behaviors were investigated. This study provides some theoretical guidance for selenium removal in WFGD, and it can also contribute to the development of specific selenium control technologies in the future.

2. MATHEMATICAL MODEL

The main physical processes considered in this model are shown in Figure 1. The upstream flue gas carrying gaseous Se, particulate-bound Se, fly ashes, and SO_2 enters the spray tower from its bottom. With the flue gas flowing upward, the SO_2 and fly ashes are absorbed or captured by droplets. For the behaviors of gaseous Se, two paths are hypothesized: path 1 is the direct absorption by droplets; path 2 is condensation on fly ashes to form particulate Se and then being captured by droplets. The occurrence of gaseous Se condensation depends on its concentration and the flue gas temperature. The selenium migration behavior (SeMB) model is built to describe the above physical processes, which is comprised of five submodels, including droplet motion, heat transfer, mass-transfer absorption, PM capture, and condensation.

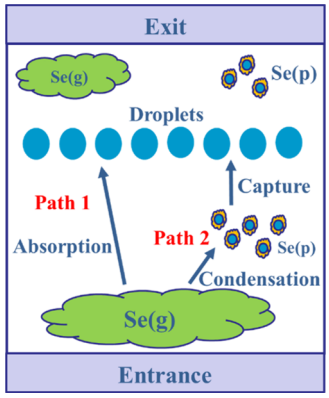

Figure 1. Physical process of selenium migration in the WFGD spray tower.

2.1. Assumptions.

The physical and chemical process in the actual WFGD spray tower is extremely complicated, involving multiphase flow, breakup or coalescence of droplets, wall rebound, and so forth. Although some of these issues can be solved by the available computational fluid dynamics method, the calculation process is time-consuming and expensive. The goal of our study is to obtain the migration behaviors of selenium and its primary affecting factors, instead of precise concentration data. Therefore, a one-dimensional model is adopted in this study. Several necessary assumptions to simplify the calculation are listed below.

1 The movement of flue gas is regarded as ideal plug flow.
2 The droplet is considered as a rigid ball in shape and falls vertically. The effects of breakup, coalescence, and wall rebound on droplets movement are ignored.
3 At each given height, the gas components, particles, and droplets are evenly distributed across the cross-section.
4 For the condensation of gaseous SeO_2, only the heterogeneous condensation via the fly ash surface is considered. The explanation is presented in Section 3.2.

2.2. Droplet Motion Submodel.

The droplets fall under the influence of gravity, buoyance, and drag.[29] The equation of droplet motion is obtained from a balance of above forces

$$\frac{\pi}{6}d_l^2\rho_l\frac{du_l}{dt} = \frac{\pi}{6}d_l^3(\rho_l - \rho_g)g - C_D\rho_g\frac{\pi}{4}d_l^2\frac{u_r^2}{2} \quad (1)$$

where d_l is the diameter of the droplet, u_l is the velocity of the droplet, u_r is the relative velocity of the droplet and the flue gas, and t is the time of droplet falling. C_D is the drag efficiency. The detailed formulas of model parameters are listed in Table S1.

The vertical space of the absorption zone is discretized into N cells based on the same time interval Δt. The height of zone i (Δz_i) is calculated as

$$\Delta z_i = \int_{t_i}^{t_i+\Delta t} u_l dt \quad (2)$$

2.3. Heat-Transfer Submodel.

After the upstream flue gas enters the spray tower, it exchanges heat with the droplets via heat convection. The heat balance equation is

$$haV(T_g - T_l) = \rho_l L c_l \Delta T_l = \rho_g Q c_g \Delta T_g \quad (3)$$

where h is the convective heat-transfer coefficient, a is the specific surface area of droplets, V is the volume of zone i, L is the volumetric liquid flow rate, and Q is the volumetric gas flow rate. c_l and c_g are the specific heat capacities of liquid and flue gas, respectively.

The convective heat-transfer coefficient h is obtained by Ranz−Marshell equation[31]

$$Nu = 2 + 0.6Re^{0.5}Pr^{0.33} = \frac{hd_l}{k} \quad (4)$$

where k is the heat-conduction coefficient.

2.4. Mass-Transfer Absorption Submodel.

The mass-transfer absorption process of SO_2 by droplets has been well studied, and the two-film theory is widely accepted to describe its absorption process.[32−34] Considering the similarities of SeO_2 and SO_2, the SeO_2 mass-transfer absorption submodel is established with reference to SO_2.

The mass-transfer equation of SeO_2 is

https://dx.doi.org/10.1021/acs.est.0c04700
Environ. Sci. Technol. 2020, 54, 16128−16137

$$\Delta G = K_g a(P_{SeO_2,g} - P_{SeO_2,l})\frac{\pi}{4}D^2\Delta z = Q\Delta c = L\Delta x \quad (5)$$

where ΔG is the mass flux of SeO_2, K_g is the globe mass-transfer coefficient, D is the diameter of the tower, Δc is the change of gas-side concentration of SeO_2, and Δx is the change of liquid-side concentration of SeO_2.·$P_{SeO_2,g}$ and $P_{SeO_2,l}$ are the partial pressures of SeO_2 in the gas side and liquid side, respectively.

Based on Henry's law, for a low-concentration gas component, its partial vapor pressure in the liquid phase is in proportion to its liquid phase concentration, that is,

$$P_{SeO_2,l} = Hx_{SeO_2} \quad (6)$$

where H is the Henry's constant.[35,36]

According to the two-film theory,[34] the mass-transfer process involves both the gas-side film and the liquid-side film. The globe mass-transfer coefficient K_g is expressed as

$$\frac{1}{K_g} = \frac{1}{k_g} + \frac{H}{Ek_l} \quad (7)$$

where k_g is the gas-side mass-transfer coefficient, k_l is the liquid-side mass-transfer coefficient, and E is the enhancement factor.

The absorption reactions in droplets are assumed to be at equilibrium.[32] The charge balance equation is expressed as

$$m_{H^+} + 2m_{Ca^{2+}} = m_{HSO_3^-} + 2m_{SO_3^{2-}} + m_{HSeO_3^-} + 2m_{SeO_3^{2-}} + m_{HCO_3^-} + 2m_{CO_3^{2-}} + m_{OH^-} + m_{Cl^-} \quad (8)$$

where m is the mole concentration and the subscripts devote specific components.

2.5. PM Capture Submodel. The size distribution of PM is set as the Rosin−Rammler expression,[37] and its cumulative distribution function is

$$F(d_p) = 1 - \exp\left(-\left(\frac{d_p}{\overline{d}}\right)^n\right) \quad (9)$$

where d_p is the size of PM, $\overline{d}$ is the characteristic size which reflects the overall particle size, and n is the uniformity index. The initial PM size is classified into 20 stages from 0.2 to 11.6 μm.

Four mechanisms for PM capture are considered in this submodel, that is, inertial impaction, thermophoresis, interception, and diffusion.[38−42] The capture efficiency by inertial impaction is[43]

$$E_{imp} = \left(\frac{St}{St + 0.35}\right)^2 \quad (10)$$

$$St = \frac{\rho_p {d_p}^2 u_r C_c}{18\mu_g d_l} \quad (11)$$

where ρ_p is the particle density, μ_g is the dynamic viscosity of flue gas, and C_c is the Cunningham correction coefficient.

The capture efficiency by thermophoresis is[39,41]

$$E_{th} = \frac{E_{Dav}}{1 + E_r} \quad (12)$$

$$E_{Dav} = \frac{4\alpha(2 + 0.6{Re_l}^{1/2}Pr^{1/3})(T_g - T_l)}{u_l d_l} \quad (13)$$

$$E_r = 0.275\lg Re + (33.26{E_{Dav}}^2 - 5.222E_{Dav} - 0.152) \quad (14)$$

The capture efficiency by interception is[44]

$$E_{in} = 4H\left(\frac{1}{\omega} + (1 + 2{Re_l}^{1/2})H\right) \quad (15)$$

where ω is the ratio of u_l and u_g and H is the ratio of d_p and d_l.

The capture efficiency by diffusion is[40]

$$E_{diff} = 2\sqrt{\frac{2}{Ped_l}} \quad (16)$$

The synthetical capture efficiency for a single droplet is calculated as[40]

$$E_{tot} = (1 - E_{im})(1 - E_{th})(1 - E_{in})(1 - E_{diff}) \quad (17)$$

The capture efficiency for the droplet group at the given zone is

$$\eta_p = \left(\frac{d_l}{D}\right)^2 \times E_{tot} \times num_{dro} \quad (18)$$

where num_{dro} is the number of droplets at the given zone.

2.6. Condensation Submodel. The supersaturation is an important parameter for the condensation process, and it is defined as

$$S = \frac{P_v}{P_{v,\infty}(T)} \quad (19)$$

where P_v is the partial vapor pressure and $P_{v,\infty}(T)$ is the vapor pressure at the gas temperature T.

The condensation phenomenon can be divided into heterogeneous condensation and homogeneous condensation. When the supersaturation exceeds 1, the crystal nuclei of gas molecules are formed on the solid surface and grow up, and this process is called as heterogeneous condensation. As for homogeneous condensation, the nuclei of molecules of condensable components are formed spontaneously without the support of the solid surface. It is reported that the critical supersaturation for homogeneous condensation is about 2−5.[45] In this model, the gaseous SeO_2 is unsaturated at the inlet of the spray tower. With the flue gas cooling down, the vapor pressure of SeO_2 decreases and the supersaturation raises. Once the supersaturation reaches 1, the heterogeneous condensation occurs, leading to the decline of the supersaturation. Thus, the supersaturation will remain slightly above 1 during the condensation process. It is reasonable to ignore the homogeneous condensation, and this is confirmed in Section 3.2.

The condensation flux of SeO_2 to particles with the diameter of $d_{p,k}$ is calculated based on Fuchs equation[16,46]

https://dx.doi.org/10.1021/acs.est.0c04700
Environ. Sci. Technol. 2020, 54, 16128−16137

$$F(k) = \begin{cases} \dfrac{2\pi d_p D_{SeO_2}(P_{SeO_2,g} - P_{SeO_2,\infty})}{RT_g} \times \dfrac{1 + Kn}{1 + 1.71Kn + 1.33Kn^2}, & d_{p,k} > 1\ \mu m \\ \dfrac{\psi\pi d_{p,k}{}^2(P_{SeO_2} - P_{SeO_2,\infty})}{\sqrt{2\pi M_{SeO_2} RT_g}}, & d_{p,k} < 1\ \mu m \end{cases} \quad (20)$$

where D_{SeO_2} is the diffusivity of SeO_2, $P_{SeO_2,\infty}$ is the vapor pressure of SeO_2, $d_{p,k}$ is the diameter of PM at the stage of k, M_{SeO_2} is the molar weight of SeO_2, and ψ is the accommodation coefficient, taken as unity.[16]

The vapor pressure of SeO_2 is obtained by Antonie equation[47]

$$P_{SeO_2,\infty} = \exp\left(25.39 - \frac{7249}{T_g - 104}\right) \quad (21)$$

For each zone, the condensation amount of SeO_2 is computed as

$$m_{cond} = \sum_{k=1}^{20} F(k)n(k)M_{SeO_2}\Delta t_g \quad (22)$$

where $n(k)$ is the number of PM at the stage k and Δt_g is the residence time of flue gas at this zone.

The logical relationship among the above five submodels is shown in Figure S1. The basic physical parameters are obtained via droplet motion submodel and heat-transfer submodel, such as flue gas temperature, droplet velocity, and so forth. The mass-transfer submodel describes the absorption process of gaseous SeO_2 and SO_2. The condensation submodel describes the transfer of gaseous SeO_2 to the PM surface, which leads to the new formation of particulate-bound Se. The PM capture submodel describes the removal process of PM and also the particulate-bound Se. The input parameters of the model are listed in Table S2. The model was computed using MATLAB R2017b.

3. RESULTS AND DISCUSSION

3.1. Model Validation. The prediction results of the SeMB model were compared with field results to validate its reliability. Two sets of field experimental data were selected which provided the information of Se(g), Se(p), and PM concentrations at the inlet and outlet of the WFGD spray tower.[24,48] The calculation results are summarized in Table 1.

Table 1. Comparison of Model Results and Reported Experimental Results[a]

	inlet[e]	outlet[e]	outlet[c]	units	data source
PM	44	1	1.1	mg/m^3	Cheng, et al.[24]
Se(g)	120	40	34.5	μg/m^3	
Se(p)	1.4	<1	2.5	μg/m^3	
PM	11	1	0.84	mg/m^3	Meji, et al.[48]
Se(g)	62.3	38.2	41.6	μg/m^3	
Se(p)	1.8	1.6	1.4	μg/m^3	

[a]Notes: subscript "e" refers to experimental results obtained from the literature; subscript "c" refers to calculation results obtained by the SeMB model.

The prediction results were all close to the experimental results. This indicated that the model could well describe the selenium migration behaviors in actual WFGD spray towers.

3.2. Typical Selenium Migration Behavior. Figure 2 shows a typical selenium migration process in a WFGD spray tower, and the main parameters are listed in Table S2. The concentrations of Se(g) and Se(p) changed sharply at the entrance section (0−1 m) and slowly decreased in the remaining part of the tower. The behavior of selenium in the entrance section is shown enlarged in Figure 2b. After the flue gas enters the tower, the saturated concentration of Se(g) [labeled as Se(g, sat)] dropped sharply because of the cooling of flue gas. When the actual Se(g) concentration reached the saturated concentration, it began to decrease and the Se(p) concentration began to increase, indicating the conversion of Se(g) to Se(p). It can be noted that the actual Se(g) concentration is slightly higher than its saturation concentration. The supersaturation of Se(g) is shown in Figure S2. The maximum supersaturation was 1.19. Thus, the conversion of Se(g) to Se(p) was mainly through heterogeneous condensation, and the effect of homogeneous condensation can be ignored.[45]

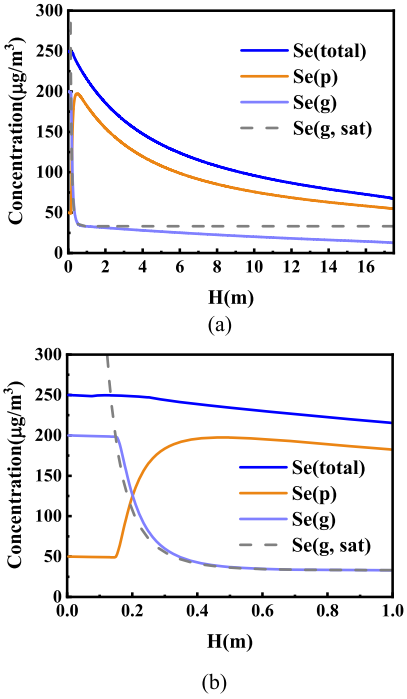

Figure 2. Typical selenium concentration curve in a WFGD spray tower: (a) Whole tower and (b) entrance section (0−1 m).

To clearly distinguish the migration path and destination of selenium in the WFGD tower, the distribution ratios of selenium in the three phases are calculated and are shown in Figure 3. Based on its form and migration path, selenium was divided into four types: "Se(g) in flue gas" referred to the gaseous selenium existing in the flue gas, "Se(p) in flue gas" referred to the particulate-bound selenium existing in the flue gas, "Se(g) in droplet" referred to the gaseous selenium that had entered the droplet by absorption, and "Se(p) in droplet" referred to the particulate-bound selenium that had entered the droplet with the capture of PMs. The latter two forms both referred to the selenium existing in droplets, but they entered

https://dx.doi.org/10.1021/acs.est.0c04700
Environ. Sci. Technol. 2020, 54, 16128−16137

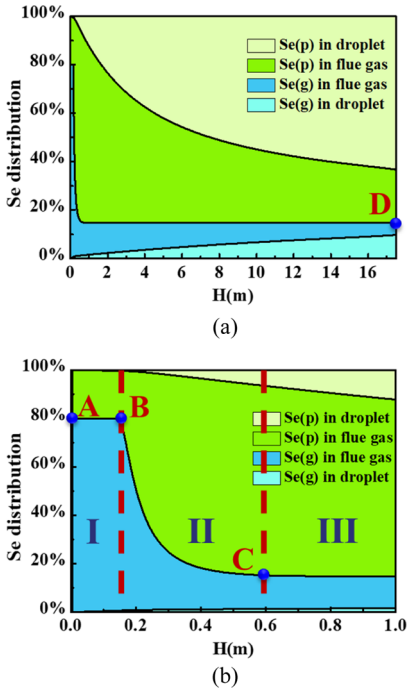

Figure 3. Typical selenium distribution in the WFGD spray tower: (a) Whole tower and (b) entrance section (0−1 m). (The colored areas represent different selenium species existing in flue gas and droplets, and the vertical height of the colored area represents the proportion of each selenium species. The black lines represent the boundaries of selenium species. The red dotted lines represent the boundaries of selenium migration stages).

droplets via different paths. From Figure 3, it can be seen that the boundary between "Se(g) in flue gas" and "Se(p) in flue gas" changed significantly in the entrance section, indicating that the gaseous Se was transformed to particulate-bound Se. According to the state of this boundary line, the migration process of selenium can be divided into three stages (shown in Figure 3b):

Stage I was from point *A* to point *B*, and it could be called as the preparation stage. The flue gas temperature decreased sharply but was higher than the dew point of SeO_2, and the condensation of SeO_2 could not occur.

Stage II was from point *B* to point *C*, and it could be called as the condensation stage. When the flue gas temperature decreased to the dew point of SeO_2, stage II started. During this stage, the concentration of Se(g) was higher than its saturation concentration. Part of Se(g) condensed on the surface of PMs, causing significant changes of Se distribution in flue gas.

Stage III was from point *C* to point *D*, and it could be called as the removal stage. The flue gas temperature remained stable. During this stage, the gaseous SeO_2 was unsaturated. Stage III occupied about 96.5% of the space in the spray tower, and the removal of selenium from flue gas mainly occurred in this stage. The specific information of these three stages is summarized in Table S3.

The migration behavior of selenium in the WFGD tower can be reflected via the SeO_2 saturation concentration curve. Figure 4 is the schematic diagram of the selenium migration process. At the entrance of the WFGD tower (point *A*), the concentration of Se(g) was assumed to be 200 $\mu g/m^3$ and the flue gas temperature was 100 °C. Point *A* was below the

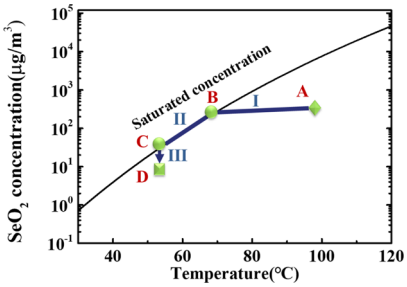

Figure 4. Schematic diagram of selenium migration behavior.

saturation concentration line. With the temperature of flue gas decreasing, the state of Se(g) reached point *B*, and condensation (stage II) started. The flue gas temperature of point *B* was about 70 °C, which was consistent with Senior's research.[26] During the condensation stage, SeO_2 in the flue gas was supersaturated, and it rapidly decreased along the saturation concentration line. When the flue gas temperature reached the droplet temperature (point *C*), it remained nearly unchanged. The remaining SeO_2 continued decreasing owing to the absorption by droplets, showing a vertical decline in stage III. Point *D* was the exit of the WFGD tower.

Above results confirmed the two paths for Se(g) migration shown in Figure 1. The removal process of selenium in the WFGD spray tower involved not only the absorption of gaseous species but also the capture of particles and the conversion from gaseous form to particulate form. This explains why the removal efficiency of Se varied greatly. It must be pointed out that the above discussion of selenium migration behavior is under a typical condition. When the state of flue gas or the WFGD operation parameters change, there will be some differences in the migration behavior of selenium, and it will be discussed in detail in Section 3.3.

3.3. Factors on Selenium Migration. Finding out the key factors on selenium migration behavior is helpful for the development of selenium control technology. From the results in Section 3.2, we can see that the condensation process of Se(g) played an important role on its migration. PM was the nuclei for heterogeneous condensation of selenium. Supersaturation was the driving force for condensation, which was decided by the Se(g) concentration and the flue temperature. Thus, five factors including PM concentration, PM size distribution, flue gas temperature, droplet temperature, and initial Se concentration are explored in this section.

3.3.1. Effect of PM Concentration. The concentration of PM in flue gas determined the surface area available for selenium condensation. Figure 5 shows the selenium distribution with different initial PM concentrations. The PM size distributions were set as consistent, and the surface area of particles was assumed to be proportional to the PM concentration. With the decrease of PM concentration from 50 to 2 mg/m^3, the condensation rate of Se(g) slowed down. When the initial PM concentration was 2 mg/m^3, stage II ended at about 4 m away from the entrance. The outlet concentration of Se and its removal rate is shown in Figure S3a. When the inlet PM concentration was in the range of 10−50 mg/m^3, the total removal efficiency of Se was almost unchanged. When the inlet PM concentration was further reduced to 2 mg/m^3, the condensation of Se(g) was hindered because of the lack of surface area. The total removal efficiency of Se decreased slightly. The PM concentration at the inlet of

https://dx.doi.org/10.1021/acs.est.0c04700
Environ. Sci. Technol. 2020, 54, 16128−16137

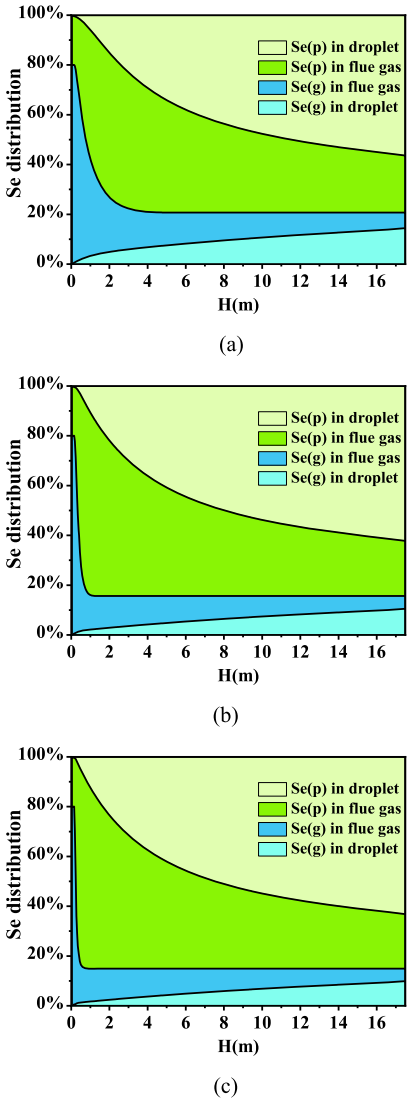

Figure 5. Selenium distribution ratio with different initial PM concentrations: (a) C_{PM} = 2 mg/m^3, (b) C_{PM} = 10 mg/m^3, and (c) C_{PM} = 50 mg/m^3.

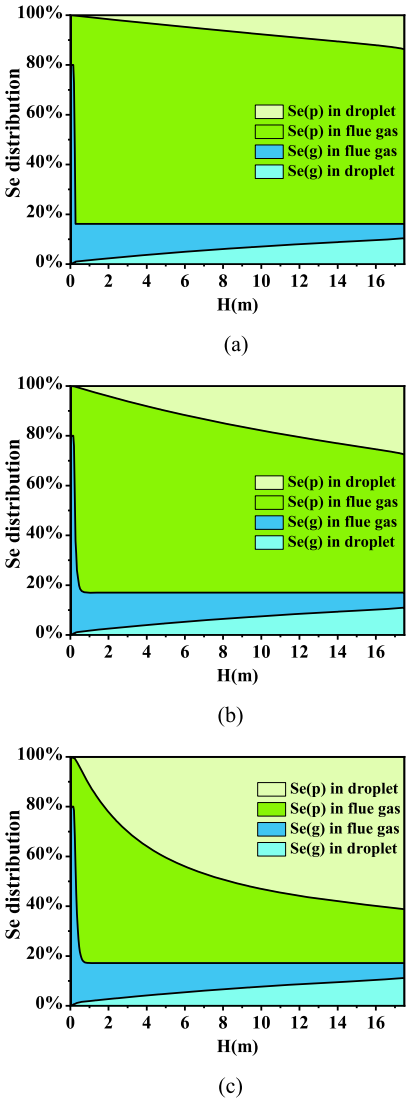

Figure 6. Selenium distribution ratio with different PM size distributions: (a) $\overline{d}$ = 1 μg/m^3, (b) $\overline{d}$ = 2 μg/m^3, and (c) $\overline{d}$ = 5 μg/m^3.

WFGD tower in actual coal-fired power plants is generally 10–40 mg/m^3.[49,50] Besides, for the situation with low PM concentration (<10 mg/m^3), the fine particles dominate in the actual flue gas, which means that the surface area of particles should be greater than the assumption by this model. It can be considered that in most cases, the concentration of PM at the inlet of the WFGD tower is sufficient for Se(g) to fully condense.

3.3.2. Effect of PM Size Distribution. PM size distribution was another factor that affected selenium condensation behavior. According to eq 20, the condensation rate of Se(g) was linearly related to d_p (while $d_p > 1$ μm) or d_p^2 (while $d_p < 1$ μm). Figure 6 shows the selenium distribution with different characteristic sizes $\overline{d}$. The condensation process slowed down with the increase of $\overline{d}$. It indicated that with the same mass concentration of PM, even though the condensation rate on large particles was higher, the number of particles decreased and the overall surface area for condensation decreased, resulting in a reduction of the whole condensation rate.

Another phenomenon can be found in Figure 6, that is, when the PM size increased, the proportion of Se(g) which finally entered the droplet increased significantly. The inertial impaction was the dominant mechanism for the capture of supermicron particles.[42,51] The trapping effect of inertial impaction was enhanced for larger particles. Therefore, with the increase of particle size, the particles and the particulate-bound selenium were easier to be captured. This phenomenon is consistent with Senior's experimental results, who injected large hydrated lime particles (with the mass mean size of 29 μm) before the inlet of WFGD tower, and the total removal of selenium was enhanced.[26]

Figure S3b shows the outlet concentration and the total removal rate of selenium. With the increase of $\overline{d}$, the concentration of Se(p) at the outlet decreased significantly and the total removal efficiency increased. The difference of inlet PM size distribution may be a key reason for the huge divergence of selenium removal rate in different units.

3.3.3. Effect of Flue Gas Temperature. Figure S4a shows the flue gas temperature curves at the entrance with various initial flue gas temperatures. Because the specific heat capacity and mass flow rate of the flue gas were much smaller than those of the droplets, the flue gas cooled down rapidly once it

https://dx.doi.org/10.1021/acs.est.0c04700
Environ. Sci. Technol. 2020, 54, 16128–16137

entered the tower, while the droplet temperature did not significantly change. The final equilibrium temperature of flue gas was not determined by its initial state but was close to the droplet temperature. Figure S4b shows the Se(g) concentrations at the entrance. There were minor differences between the condensation processes of Se(g) under different flue gas temperatures. The only difference was that the condensation of Se(g) occurred slightly earlier at lower inlet flue gas temperature because the dew-point temperature reached faster. However, owing to the same droplet temperature, the Se(g) concentrations at the end of stage II were the same. It can be seen from Figure S3c that the initial flue gas temperature had little effect on the concentration of Se at the outlet.

3.3.4. Effect of Droplet Temperature. Figure 7 shows the selenium distribution with different droplet temperatures.

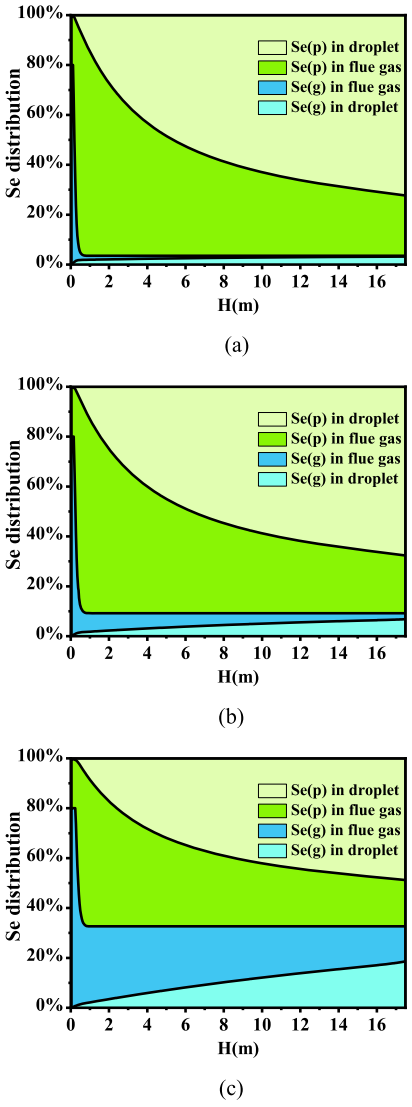

Figure 7. Selenium distribution ratio with different droplet temperatures: (a) T_l = 40 °C, (b) T_l = 50 °C, and (c) T_l = 60 °C.

When the droplet temperature decreased, the proportion of Se(g) in flue gas at the end of stage II dramatically reduced. This is because the saturation concentration of Se(g) was related to the flue gas temperature, and the flue gas temperature was largely determined by the droplet temperature. The flue gas temperature reached the droplet temperature at the end of stage II, and the saturation Se(g) concentration decreased accordingly, causing more Se(g) to condense on the particles. When the droplet temperature was 40 °C, the saturation concentration of Se(g) was 3.9 $\mu g/m^3$, and thus almost all Se(g) was converted into Se(p). The outlet concentration of Se and its removal efficiency are shown in Figure S3d. The total Se removal efficiency increased with the decrease of droplet temperature.

3.3.5. Effect of Initial Se Concentration. The Se concentration in flue gas largely depends on the Se content in coal. The Se content in coal worldwide varies from 0.2 to 4 $\mu g/kg$.[S2] The average concentration of Se in Chinese coal is between 0.17 and 9.71 $\mu g/kg$.[S3] Besides, the control effects on Se by upstream APCDs are different among various coal-fired units. Therefore, the Se concentrations at the inlet of WFGD towers are different. Figure 8 shows the concentrations of

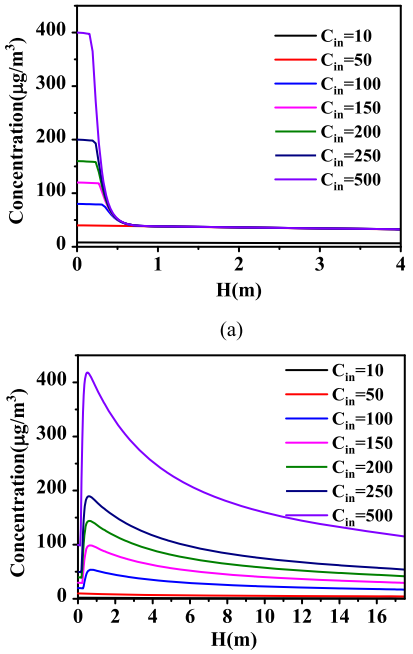

Figure 8. Effect of inlet selenium concentration on selenium behavior: (a) Concentration of gaseous selenium and (b) concentration of particulate selenium.

Se(g) and Se(p) in the entrance section with various initial Se concentrations (C_{in}). When the initial Se concentration was 100−500 $\mu g/m^3$, Se(g) rapidly decreased to the same value, which was its saturation concentration. However, when the Se concentration was below 50 $\mu g/m^3$, there was no conversion of Se(g) to Se(p). This is because the Se(g) concentration was lower than its saturation concentration at the corresponding temperature, leading to the lack of driving force for condensation. In this situation, the typical three-stage Se migration process can be simplified to one removal stage, that is, Se(g) and Se(p) were removed by droplets independently and the condensation process can be ignored. Figure S3e shows the outlet concentration of Se and its removal efficiency. With the increase of the initial Se concentration, the outlet Se(g) concentration remained unchanged and the Se(p) concentration increased. The removal efficiency increased from 62 to 74% and kept unchanged for higher initial Se concentration.

https://dx.doi.org/10.1021/acs.est.0c04700
Environ. Sci. Technol. 2020, 54, 16128−16137

The influence of the initial flue gas temperature, droplet temperature, and Se concentration can be clearly reflected in the Se(g) condensation schematic diagram, which is shown in Figure S5. The initial flue gas temperature decided the horizonal position of point *A*. The initial droplet temperature decided the length from point *B* to point *C*. The initial Se concentration decided the vertical position of point *A*.

The removal efficiency of selenium in WFGD towers is closely related to its species in flue gas. Among the five factors discussed in Section 3.3, the PM size distribution and the slurry temperature showed significant effects on the migration process of selenium. According to these results, two specific methods are potential to enhance the selenium removal in WFGD towers. The first one is to aggregate the particles at the inlet of the tower and to make Se(p) easier to be captured. The second one is to cool down the slurry to improve the condensation of Se(g), and this method is suitable for WFGD systems with high PM removal efficiency.

■ ASSOCIATED CONTENT

Supporting Information

The Supporting Information is available free of charge at https://pubs.acs.org/doi/10.1021/acs.est.0c04700.

> Model parameters, input parameters, architecture diagram of the model, supersaturation of SeO_2, outlet Se concentration and removal efficiency, effect of the inlet flue gas temperature, and schematic diagram of Se migration behaviors under different conditions (PDF)

■ AUTHOR INFORMATION

Corresponding Authors

Guangqian Luo − *State Key Laboratory of Coal Combustion (SKLCC), School of Energy and Power Engineering, Huazhong University of Science and Technology, Wuhan, Hubei 430074, China;* orcid.org/0000-0003-4697-4698; Phone: +86-27-87545526; Email: guangqian.luo@mail.hust.edu.cn

Hong Yao − *State Key Laboratory of Coal Combustion (SKLCC), School of Energy and Power Engineering, Huazhong University of Science and Technology, Wuhan, Hubei 430074, China;* orcid.org/0000-0002-2836-7803; Email: hyao@hust.edu.cn

Authors

Renjie Zou − *State Key Laboratory of Coal Combustion (SKLCC), School of Energy and Power Engineering, Huazhong University of Science and Technology, Wuhan, Hubei 430074, China;* orcid.org/0000-0003-3146-4716

Can Fang − *State Key Laboratory of Coal Combustion (SKLCC), School of Energy and Power Engineering, Huazhong University of Science and Technology, Wuhan, Hubei 430074, China*

Haoyu Zhang − *State Key Laboratory of Coal Combustion (SKLCC), School of Energy and Power Engineering, Huazhong University of Science and Technology, Wuhan, Hubei 430074, China*

Zehua Li − *State Key Laboratory of Coal Combustion (SKLCC), School of Energy and Power Engineering, Huazhong University of Science and Technology, Wuhan, Hubei 430074, China;* orcid.org/0000-0003-2518-9287

Hongyun Hu − *State Key Laboratory of Coal Combustion (SKLCC), School of Energy and Power Engineering, Huazhong University of Science and Technology, Wuhan, Hubei 430074, China;* orcid.org/0000-0002-0218-2130

Xian Li − *State Key Laboratory of Coal Combustion (SKLCC), School of Energy and Power Engineering, Huazhong University of Science and Technology, Wuhan, Hubei 430074, China;* orcid.org/0000-0002-5387-4647

Complete contact information is available at: https://pubs.acs.org/10.1021/acs.est.0c04700

Notes

The authors declare no competing financial interest.

■ ACKNOWLEDGMENTS

The National Key Research and Development Program of China (2018YFB0605103) and the Chinese National Natural Science Foundation (51776084) are gratefully acknowledged.

■ NOMENCLATURE

a	specific surface area, m^2/m^3
c	specific heat capacity, J/(Kg·K), or gas-side concentration, mol/m^3
C_c	Cunningham correction coefficient, dimensionless
C_D	drag coefficient, dimensionless
d	diameter, m
$\overline{d}$	characteristic size, m
D	diameter of spray tower, m, or diffusivity, m^2/s
E	capture efficiency of PM by single droplet, dimensionless, or enhancement factor, dimensionless
$F(d)$	cumulative distribution fraction of particle with the diameter of d, dimensionless
F	condensation flux to particle of size $d_{p,k}$, mol/(s·1)
g	acceleration of gravity, m^2/s
G	mass flux, mol/s
h	convective heat-transfer coefficient, $W/(m^2·K)$
H	Henry's constant, $Pa·m^3/mol$, or ratio of d_p and d_l, dimensionless
k	heat-conduction coefficient, W/(m·K), or mass transfer coefficient, m/s
K	globe mass transfer coefficient, m/s
Kn	Knudsen number, dimensionless
L	volumetric liquid flow rate, m^3/s
m	mole concentration of charge, mol/m^3
M	molar weight, g/mol
m_{cond}	mass flus of condensation, g
n	uniformity index, dimensionless, or number
Nu	Nusselt number, dimensionless
P	partial pressure, Pa
Pe	Peclet number, dimensionless
Pr	Prandtl number, dimensionless
Q	volumetric gas flow rate, m^3/s
R	universal gas constant, J/(mol·K)
Re	Reynolds number, dimensionless
S	supersaturation, dimensionless
St	Stokes number, dimensionless
t	time, s
T	temperature, K
u	velocity, m/s
V	volume of calculated zone, m^3
x	liquid-side concentration, mol/m^3
z	height of calculated zone, m
α	simplified coefficient in E_{th} calculation
η	capture efficiency for the droplet group, dimensionless

μ dynamic viscosity, Pa·s
ρ density, kg/m^3
ψ accommodation coefficient, dimensionless
ω ratio of u_l and u_g, dimensionless
Dav thermophoresis capture efficiency proposed by Davenport
diff diffusion mechanism
dro droplet
g flue gas
i number of calculated zone
imp inertial impaction mechanism
in interception mechanism or inlet
k particle stage
l liquid or droplet
p particulate matter
r relative velocity
th thermophoresis mechanism
tot total capture efficiency
v vapor
∞ vapor pressure

REFERENCES

(1) Ma, L.; Fang, Q.; Lv, D.; Zhang, C.; Chen, Y.; Chen, G.; Duan, X.; Wang, X. Reducing NOx Emissions for a 600 MWe Down-Fired Pulverized-Coal Utility Boiler by Applying a Novel Combustion System. *Environ. Sci. Technol.* **2015**, *49*, 13040−13049.

(2) Liu, X.; Xu, Y.; Qi, J.; Wang, H.; Zhang, T.; Xu, M. Effects of kaolin-limestone blended additive on the formation and emission of particulate matter: Field study on a 1000 MW coal-firing power station. *J. Hazard. Mater.* **2020**, *399*, 123091.

(3) Xu, Y.; Luo, G.; Pang, Q.; He, S.; Deng, F.; Xu, Y.; Yao, H. Adsorption and catalytic oxidation of elemental mercury over regenerable magnetic Fe Ce mixed oxides modified by non-thermal plasma treatment. *Chem. Eng. J.* **2019**, *358*, 1454−1463.

(4) Xu, Y.; Luo, G.; Zhou, M.; Zhang, Q.; Li, Z.; Zhang, S. Natural ferruginous manganese ore for efficient immobilization of elemental mercury from coal combustion flue gas. *Fuel* **2021**, *283*, 118946.

(5) Ouyang, J.; Hong, D.; Jiang, L.; Li, Z.; Liu, H.; Luo, G.; Yao, H. Effect of CO_2 and H_2O on Char Properties. Part 1: Pyrolysis Char Structure and Reactivity. *Energy Fuels* **2020**, *34*, 4243−4250.

(6) Zhao, S.; Duan, Y.; Li, C.; Li, Y.; Chen, C.; Liu, M.; Lu, J. Partitioning and emission of hazardous trace elements in a 100 MW coal-fired power plant equipped with selective catalytic reduction, electrostatic precipitator, and wet flue gas desulfurization. *Energy Fuels* **2017**, *31*, 12383−12389.

(7) Zhao, S.; Duan, Y.; Li, Y.; Liu, M.; Lu, J.; Ding, Y.; Gu, X.; Tao, J.; Du, M. Emission characteristic and transformation mechanism of hazardous trace elements in a coal-fired power plant. *Fuel* **2018**, *214*, 597−606.

(8) Zhao, S.; Duan, Y.; Lu, J.; Liu, S.; Pudasainee, D.; Gupta, R.; Liu, M.; Lu, J. Enrichment characteristics, thermal stability and volatility of hazardous trace elements in fly ash from a coal-fired power plant. *Fuel* **2018**, *225*, 490−498.

(9) Ratafia-Brown, J. A. Overview of trace element partitioning in flames and furnaces of utility coal-fired boilers. *Fuel Process. Technol.* **1994**, *39*, 139−157.

(10) Senior, C. L.; Bool, L. E.; Morency, J. R. Laboratory study of trace element vaporization from combustion of pulverized coal. *Fuel Process. Technol.* **2000**, *63*, 109−124.

(11) Brandt, J. E.; Bernhardt, E. S.; Dwyer, G. S.; Di Giulio, R. T. Selenium ecotoxicology in freshwater lakes receiving coal combustion residual effluents: a North Carolina example. *Environ. Sci. Technol.* **2017**, *51*, 2418−2426.

(12) Lemly, A. D. Symptoms and implications of selenium toxicity in fish: the Belews Lake case example. *Aquat. Toxicol.* **2002**, *57*, 39−49.

(13) *National Emission Standards for Hazardous Air Pollutants from Coal and Oil-Fired Electric Utility Steam Generating Units and Standards of Performance for Fossil-Fuel-Fired Electric Utility, Industrial-Commercial-Institutional, and Small Industrial- Commercial-Institutional Steam Generating Units; Technical Correction*; Environmental Protection Agency, 2016.

(14) Yan, R.; Gauthier, D.; Flamant, G.; Peraudeau, G.; Lu, J.; Zheng, C. Fate of selenium in coal combustion: volatilization and speciation in the flue gas. *Environ. Sci. Technol.* **2001**, *35*, 1406−1410.

(15) Seames, W. S.; Wendt, J. O. L. Regimes of association of arsenic and selenium during pulverized coal combustion. *Proc. Combust. Inst.* **2007**, *31*, 2839−2846.

(16) Senior, C.; Otten, B. V.; Wendt, J. O. L.; Sarofim, A. Modeling the behavior of selenium in pulverized-coal combustion systems. *Combust. Flame* **2010**, *157*, 2095−2105.

(17) Wang, J.; Zhang, Y.; Wang, T.; Xu, H.; Pan, W.-P. Effect of modified fly ash injection on As, Se, and Pb emissions in coal-fired power plant. *Chem. Eng. J.* **2020**, *380*, 122561.

(18) Wang, J.; Zhang, Y.; Liu, Z.; Gu, Y.; Norris, P.; Xu, H.; Pan, W.-P. Coeffect of air pollution control devices on trace element emissions in an ultralow emission coal-fired power plant. *Energy Fuels* **2018**, *33*, 248−256.

(19) Chang, L.; Yang, J.; Zhao, Y.; Liu, H.; Zhang, J.; Zheng, C. Behavior and fate of As, Se, and Cd in an ultra-low emission coal-fired power plant. *J. Clean. Prod.* **2019**, *209*, 722−730.

(20) Córdoba, P. Partitioning and speciation of selenium in wet limestone flue gas desulphurisation systems: A review. *Fuel* **2017**, *202*, 184−195.

(21) Córdoba, P. Status of Flue Gas Desulphurisation (FGD) systems from coal-fired power plants: Overview of the physic-chemical control processes of wet limestone FGDs. *Fuel* **2015**, *144*, 274−286.

(22) Ortiz, F. J. G.; Vidal, F.; Ollero, P.; Salvador, L.; Cortes, V. Pilot-plant technical assessment of wet flue gas desulfurization using limestone. *Ind. Eng. Chem. Res.* **2006**, *45*, 1466−1477.

(23) Tang, Q.; Liu, G.; Yan, Z.; Sun, R. Distribution and fate of environmentally sensitive elements (arsenic, mercury, stibium and selenium) in coal-fired power plants at Huainan, Anhui, China. *Fuel* **2012**, *95*, 334−339.

(24) Cheng, C.-M.; Hack, P.; Chu, P.; Chang, Y.-N.; Lin, T.-Y.; Ko, C.-S.; Chiang, P.-H.; He, C.-C.; Lai, Y.-M.; Pan, W.-P. Partitioning of mercury, arsenic, selenium, boron, and chloride in a full-scale coal combustion process equipped with selective catalytic reduction, electrostatic precipitation, and flue gas desulfurization systems. *Energy Fuels* **2009**, *23*, 4805−4816.

(25) Zou, R.; Zhang, H.; Luo, G.; Fang, C.; Shi, M.; Hu, H.; Li, X.; Yao, H. Selenium migration behaviors in wet flue gas desulfurization slurry and an in-situ treatment approach. *Chem. Eng. J.* **2020**, *385*, 123891.

(26) Senior, C. L.; Tyree, C. A.; Meeks, N. D.; Acharya, C.; McCain, J. D.; Cushing, K. M. Selenium partitioning and removal across a wet FGD scrubber at a coal-fired power plant. *Environ. Sci. Technol.* **2015**, *49*, 14376−14382.

(27) Senior, C.; Blyther, G.; Chu, P. Multi-media emissions of selenium from coal-fired electric utility boilers. *Air Quality VIII*: Crystal City, VA, 2011.

(28) Yaws, C. L. *Yaws Handbook of Antoine Coefficients for Vapor Pressure*, 2009.

(29) Zhu, J.; Ye, S.-c.; Bai, J.; Wu, Z.-y.; Liu, Z.-h.; Yang, Y.-f. A concise algorithm for calculating absorption height in spray tower for wet limestone−gypsum flue gas desulfurization. *Fuel Process. Technol.* **2015**, *129*, 15−23.

(30) Chen, B.; Sun, F.; Gao, M.; Shi, Y. A 1-D model of spraying performance for wet flue gas desulfurization scrubber based on predicted slurry temperature. *Appl. Therm. Eng.* **2019**, *155*, 259−266.

(31) Ranz, W. E.; Marshall, W. R. Evaporation from drops. *Chem. Eng. Prog.* **1952**, *48*, 141−146.

(32) Marocco, L. Modeling of the fluid dynamics and SO_2 absorption in a gas−liquid reactor. *Chem. Eng. J.* **2010**, *162*, 217−226.

https://dx.doi.org/10.1021/acs.est.0c04700
Environ. Sci. Technol. 2020, 54, 16128−16137

(33) Neveux, T.; Le Moullec, Y. Wet Industrial Flue Gas Desulfurization Unit: Model Development and Validation on Industrial Data. *Ind. Eng. Chem. Res.* **2011**, *50*, 7579−7592.
(34) Whitman, W. G. The two-film theory of gas absorption. *Int. J. Heat Mass Transfer* **1962**, *5*, 429−433.
(35) Henry, W. III Experiments on the quantity of gases absorbed by water, at different temperatures, and under different pressures. *Trans. Roy. Soc. Lond.* **1803**, *93*, 29−274.
(36) Sander, R. Compilation of Henry's law constants (version 4.0) for water as solvent. *Atmos. Chem. Phys.* **2015**, *15*, 4399−4981.
(37) Liu, S.; Yang, H.; Zhang, Z.; Chen, J.; Chen, C.; Guo, T.; Cao, Y.; Jia, W. Emission Characteristics of Fine Particles from Wet Flue Gas Desulfurization System Using a Cascade of Double Towers. *Aerosol Air Qual. Res.* **2018**, *18*, 1901−1909.
(38) Wang, A.; Song, Q.; Yao, Q. Study on inertial capture of particles by a droplet in a wide Reynolds number range. *J. Aerosol Sci.* **2016**, *93*, 1−15.
(39) Wang, A.; Song, Q.; Yao, Q. Thermophoretic capture of submicron particles by a droplet. *Atmos. Environ.* **2016**, *147*, 157−165.
(40) Wang, S.; Wang, J.; Song, C.; Wen, J. Numerical investigation on urea particle removal in a spray scrubber using particle capture theory. *Chem. Eng. Res. Des.* **2019**, *145*, 150−158.
(41) Davenport, H. M.; Peters, L. K. Field studies of atmospheric particulate concentration changes during precipitation. *Atmos. Environ.* **1978**, *12*, 997−1008.
(42) Kim, H. T.; Jung, C. H.; Oh, S. N.; Lee, K. W. Particle Removal Efficiency of Gravitational Wet Scrubber Considering Diffusion, Interception, and Impaction. *Environ. Eng. Sci.* **2001**, *18*, 125−136.
(43) Rafidi, N.; Brogaard, F.; Chen, L.; Håkansson, R.; Tabikh, A. CFD and experimental studies on capture of fine particles by liquid droplets in open spray towers. *Sustainable Environ. Res.* **2018**, *28*, 382−388.
(44) Carotenuto, C.; Di Natale, F.; Lancia, A. Wet electrostatic scrubbers for the abatement of submicronic particulate. *Chem. Eng. J.* **2010**, *165*, 35−45.
(45) Tammaro, M.; Di Natale, F.; Salluzzo, A.; Lancia, A. Heterogeneous condensation of submicron particles in a growth tube. *Chem. Eng. Sci.* **2012**, *74*, 124−134.
(46) Fuchs, N. A. *Evaporation and Droplet Growth in Gaseous Media*, 1959.
(47) Xu, W.; Song, Q.; Song, G.; Yao, Q. The vapor pressure of Se and SeO_2 measurement using thermogravimetric analysis. *Thermochim. Acta* **2020**, *683*, 178480.
(48) Meji, R. Trace element behavior in coal-fired power plants. *Fuel Process. Technol.* **1994**, *39*, 199−217.
(49) Wu, B.; Tian, H.; Hao, Y.; Liu, S.; Liu, X.; Liu, W.; Bai, X.; Liang, W.; Lin, S.; Wu, Y.; Shao, P.; Liu, H.; Zhu, C. Effects of Wet Flue Gas Desulfurization and Wet Electrostatic Precipitators on Emission Characteristics of Particulate Matter and Its Ionic Compositions from Four 300 MW Level Ultralow Coal-Fired Power Plants. *Environ. Sci. Technol.* **2018**, *52*, 14015−14026.
(50) Qi, Z.; Li, J.; Wu, D.; Xie, W.; Li, X.; Liu, C. Particulate Matter Emission Characteristics and Removal Efficiencies of a Low-Low Temperature Electrostatic Precipitator. *Energy Fuels* **2017**, *31*, 1741−1746.
(51) Huang, Y.; Zheng, C.; Li, Q.; Zhang, J.; Guo, Y.; Zhang, Y.; Gao, X. Numerical simulation of the simultaneous removal of particulate matter in a wet flue gas desulfurization system. *Environ. Sci. Pollut. Res. Int.* **2020**, *27*, 1598−1607.
(52) Xu, M. Status of trace element emission in a coal combustion process: a review. *Fuel Process. Technol.* **2004**, *85*, 215−237.
(53) Hu, J.; Sun, Q.; He, H. Thermal effects from the release of selenium from a coal combustion during high-temperature processing: a review. *Environ. Sci. Pollut. Res. Int.* **2018**, *25*, 13470−13478.

https://dx.doi.org/10.1021/acs.est.0c04700
Environ. Sci. Technol. 2020, 54, 16128−16137